Check for updates

Cite this: *RSC Adv.*, 2021, **11**, 33373

Enhanced photocatalytic degradation of organic contaminants over a CuO/g-C$_3$N$_4$ p−n heterojunction under visible light irradiation†

Lejie Zhu,‡[a] Jianmin Luo, [ID] ‡*[a] Guohui Dong, [ID] *[b] Yun Lu,[c] Yinlong Lai,*[a] Jun Liu,[d] Guanmei Chen[a] and Yi Zhang[a]

As a kind of metal-free organic semiconductor photocatalyst, g-C$_3$N$_4$ has been widely explored for use in photocatalysis. However, the low quantum yield, small absorption range, and poor conductivity limit its large-scale application. Introducing another kind of semiconductor, particularly an oxide semiconductor, can result in some unexpected properties, such as an improved change transfer, enhanced light absorption, and better conductivity. In this work, CuO/g-C$_3$N$_4$ is successfully prepared through an impregnation and post-calcination method. A series of measurements support the formation of an organic-inorganic hybrid p−n heterojunction at the CuO (p-type) and g-C$_3$N$_4$ (n-type) interface. Furthermore, the photoactivity of the composite is evaluated *via* photocatalytic NO removal and the visible degradation of rhodamine B (RhB). Results show that the photocatalytic properties of CuO/g-C$_3$N$_4$ are almost twice as high as those of g-C$_3$N$_4$. In comparative tests, the photocatalytic degradation performance of Mix-CuO/g-C$_3$N$_4$ (the mixture of CuO and g-C$_3$N$_4$ nanosheets prepared by mechanically mixing) is even lower than that of pure g-C$_3$N$_4$. The degradation of RhB is only 19.7% under visible light after 30 min of irradiation. The improvement in the photoactivity of CuO/g-C$_3$N$_4$ results from the built-in electric field close to the formed p−n heterojunction, which switches the electron transfer mechanism from a double-charge transfer mechanism to a Z-scheme mechanism. In addition, the formed p−n heterojunction favors charge transfer, and thus the photocatalytic performance is significantly improved.

1. Introduction

Recently, graphitic carbon nitride (g-C$_3$N$_4$) has received significant attention owing to its distinctive two dimensional (2D) graphitic structure, non-toxic nature, outstanding chemical stability, as well as its low cost. In addition, g-C$_3$N$_4$ has great potential for use in fluorescence sensors, supercapacitors,[1,2] catalyst carriers, trace metal ion detection and so on. In 2009, Wang's group found that g-C$_3$N$_4$ was capable of photocatalytically decomposing water under visible light.[3] After that, more and more efforts have been directed at exploring the photocatalytic performance of g-C$_3$N$_4$.[4–6] As a kind of metal-free organic semiconductor photocatalyst, g-C$_3$N$_4$ has many desirable properties,

such as a suitable band-gap, visible light harvesting, and can be easily modified. However, g-C$_3$N$_4$ still has many drawbacks, for example, a small absorption range (<450 nm), the rapid recombination of photogenerated carriers, a low quantum yield, and poor conductivity.[7] Therefore, it is of great importance to modify g-C$_3$N$_4$ to broaden its photoresponse, enhance the photoinduced electrons–holes separation, as well as improving the efficiency and conductivity. In the field of photocatalysis, many strategies can be used to raise the photocatalytic performance of catalysts, including introducing defects, depositing noble metals, and nonmetal or metal doping.[8–14]

Alternatively, semiconductor coupling is a representative way to improve the photoactivity. The formed heterojunction at the interface of two semiconductors favors the separation and transfer of photogenerated carriers, and thus enhances the photocatalytic performance.[10] In addition, introducing an oxide semiconductor can also introduce some unexpected properties, such as enhanced light adsorption and better conductivity.[15,16] Among these oxide semiconductors, cupric oxide (CuO) has attracted the attention of more and more researchers owing to its excellent properties, such as its low cost, it is easily obtained, and it is environmentally friendly.[17,18] Moreover, CuO is a p-type semiconductor, which has a very small band-gap (1.2–1.7 eV).

[a]College of Chemistry and Civil Engineering, Shaoguan University, Shaoguan, 512005, PR China. E-mail: xxyljm@163.com; chemlaiyinlong@163.com

[b]School of Environmental Science and Engineering, Shanxi University of Science and Technology, Xi'an, 710021, PR China. E-mail: dongguohui@sust.edu.cn

[c]Xinjiang Teacher College, Urumqi, 830011, PR China

[d]Chengdu Customs Technology Center, Chengdu, 610041, PR China

† Electronic supplementary information (ESI) available. See DOI: 10.1039/d1ra05329a

‡ These authors contributed equally.

CuO can capture the majority of solar energy and the photo-generated carriers are able to efficiently separate under low solar light energy. More importantly, CuO is a p-type semi-conductor, C_3N_4 is a n-type, and both of them can form a heterojunction, accelerating the charge transfer.[19]

In this work, a CuO/g-C_3N_4 heterojunction was successfully prepared through an impregnation method by following the protocol developed in our previous work.[20] In particular, g-C_3N_4 was used as the precursor, and copper acetate as the Cu source. The photocatalytic performance of the composite was evaluated through the visible degradation of rhodamine B (RhB) and NO removal. In addition, the mechanism for the enhancement of the photoactivity is also thoroughly discussed.

2. Experimental section

2.1. Preparation of the catalysts

Copper acetate and anhydrous ethanol were purchased from Adamas-beta. Melamine ($C_3H_6N_6$), cyanuric acid ($C_3H_3N_3O_3$), and perchloric acid were obtained from Sigma-Aldrich. Tert butanol (TBA) and p-benzoquinone (PBQ) were supplied by Aladdin. Ultrapure water (18.25 MΩ cm) was used throughout the experiment. g-C_3N_4 was prepared through calcination as reported in our previous work.[20] Typically, cyanuric acid (2 g) and melamine (1 g) were placed into a beaker, and then anhydrous ethanol (20 mL) was added to the beaker under vigorous stirring. After a period of 3 h, the mixture was heated at 60 °C until all the anhydrous ethanol completely evaporated. Then, the obtained solids in the beaker were transferred to a crucible, and were subsequently calcined at 520 °C for 4 h. After the calcination, the color of the solids changed to yellow, implying g-C_3N_4 had been produced. To prepare CuO-g-C_3N_4, g-C_3N_4 (1 g) was first placed into a round bottom flask, then 100 mL copper acetate solution (0.1 M) was also introduced. This mixture was kept under acute ultrasonication for 1 h and stirred for another 3 h at room temperature. Subsequently, the mixture was washed using distilled water and absolute ethyl alcohol using centrifugation six times to remove the unreacted raw materials. Subsequently, the mixture was treated using vacuum freeze-drying for 24 h. The dried powder was calcined at 500 °C for 2 h, and the final sample was denoted as CuO-g-C_3N_4. The synthesis of samples with different amounts of CuO loading and bare CuO can be found in the ESI.†

2.2. Characterizations

The crystalline structures of all samples were characterized using X-ray diffractometry (XRD, Bruker D8). The X-ray source was Cu Kα and the scanning range and rate were 10–80° and 2° min^{-1}, respectively. The wavelength was 0.15418 nm. The morphology of the photocatalysts was determined using high resolution transmission electron microscopy (HRTEM, Japan JEOL-JEM type 2100) and scanning electron microscopy (SEM, Zeiss Supra 55VP). The optical properties of all samples were measured through ultraviolet-visible diffusion reflectance spectra (UV-vis DRS, Shimadzu Solid Spec-3700DUV), using $BaSO_4$ as the reference and the scanning range was 200–800 nm.

Inductively coupled plasma optical emission spectrometry (ICP-OES, ICP-ES725) was used to detect the content of the Cu element. Typically, 0.1 g of the sample was added to a Teflon crucible, 5 mL of perchloric acid was introduced subsequently and it was evaporated to total dryness. After that, 15 mL of aqua regia was added to the crucible and treated for half an hour. The mixture was placed in a 100 mL volumetric flask after cooling to room temperature for further measurements. The surface element composition and chemical state of the samples were analyzed using X-ray photoelectron spectroscopy (XPS, VG Microtech MT500). Al Kα is the diffraction source, and C 1s = 284.6 eV acts as the standard calibration binding energy.

The photoelectrochemical (PEC) performance of all samples was conducted through a traditional three electrode configuration on an electrochemical station (CHI 660C). A Pt plate (1 × 1 cm^2) and saturated calomel electrode were used as the counter electrode and reference electrode, respectively, KCl solution (0.1 M) was used as the electrolyte, the light source was supplied by a 300 W xenon lamp (λ > 420 nm), and the external bias voltage was −0.5 V.

The specific preparation procedures for the working electrode are as follows. Firstly, indium tin oxide (ITO) glasses were ultrasonically cleaned using anhydrous ethanol, ultrapure water, and then dried under an N_2 flow. Secondly, 20 mg of the sample was placed in an agate mortar, and 4 mL of naphthol was added quickly. After the samples were ground into a smooth paste they were scraped using a scraper and put onto the ITO glass. During the process, the actual contact area should remain the same size. Finally, the ITO glasses were put in an oven and treated at 60 °C for 2 h.

2.3 Photoactivity measurements

The photoactivity of the samples was evaluated using the photocatalytic degradation of RhB under visible light. The light source was supplied using a 300 W xenon lamp (λ > 420 nm). In a typical photocatalytic process, 0.1 g of the photocatalyst was added in a RhB solution (100 mL, 5 ppm). Then, the beaker containing the catalyst was treated in an ultrasonic bath for 10 min to ensure the uniform dispersion of the photocatalyst. The mixture was stirred for 1 h under dark conditions to reach the adsorption equilibrium at the interface between the RhB molecule and the photocatalyst. Then, 5 mL of the RhB solution was centrifuged and measured at 553 nm using the UV-vis spectrophotometer at a given time. In all measurements, the lamp was kept on for 30 min before the photocatalytic reactions in order to obtain a stable illumination.

A continuous flow reactor (30 × 15 × 10 cm) was used for the photocatalytic removal of NO, a visible LED lamp (300 W) equipped with a 420 nm cut-off filter was used as the simulated visible light source. Firstly, 0.1 g of the sample photocatalyst was homogeneously deposited on the surface of a circular glass sample dish (R = 12 cm) using sonication and evaporation. The concentration of NO was adjusted to 600 ppb and the flow rate was kept at 1.0 L min^{-1}. Then, the dish was moved into the reactor. After the adsorption–desorption equilibrium of NO over a photocatalyst was reached, the LED lamp was turned on to

initiate the photocatalytic removal of NO. The concentration of NO after photocatalytic removal was measured online using a chemiluminescence NO analyzer (Thermo, 42i).

3. Results and discussion

As shown in Fig. 1a, these two samples both have characteristic peaks at $2\theta = 13.0°$ and $27.4°$. Among them, the peak intensity at $2\theta = 13.0°$ is relatively weak, which represent the (100) plane of g-C_3N_4, indicating the irregular arrangement of the three-azine ring in the structure of g-C_3N_4.[21] In addition, the peak at $2\theta = 27.4°$ is very strong, which is assigned to the (002) plane of g-C_3N_4 and is formed through the stacking of g-C_3N_4 with an interlayer distance of about 0.336 nm.[22,23] More importantly, for CuO-g-C_3N_4, the peak at $2\theta = 13.0°$ is weaker than that of g-C_3N_4. Meanwhile, the peak at $2\theta = 27.4°$ shifts towards a higher angle $(\Delta 2\theta = 0.2°)$. These two phenomena suggest the successful preparation of the CuO-g-C_3N_4 composite, the combination process disrupts the regular arrangement of the three-azine ring and affects the stacking between each layer. In addition, peaks belonging to CuO are not detected in the XRD pattern of CuO-g-C_3N_4. Two possible reasons could be: (i) the content of CuO in CuO-g-C_3N_4 is too low to be observed; (ii) CuO is coated by g-C_3N_4 in CuO-g-C_3N_4. Furthermore, the characteristics of bare CuO were tested (Fig. S2, ESI†). It was shown that CuO can be prepared successfully using the same conditions as for CuO-g-C_3N_4. Fig. 2a shows that g-C_3N_4 is composed of ultrathin nanosheets. The corresponding selected area (electron) diffraction (SAED) pattern in Fig. 2b proves that g-C_3N_4 is amorphous. The transmission electron microscopy (TEM) image in Fig. 2c shows that the size of g-C_3N_4 becomes finer after calcination with CuO. According to the particle size distribution curve (Fig. S1†), the size of the sample ranges from 20 to 60 nm, fitting the normal distribution. The size of about 40 nm accounts for the highest percentage (25.7%). These nanoscale particles possess many special characteristics, such as the surface effect and quantum size effect, which are beneficial to promoting the photocatalytic performance. In Fig. 2d, the interplanar spacing of black particles is 0.25 nm, corresponding to the (111) plane of CuO.[24,25] From Fig. S2d (in the ESI†), we can see that the CuO interplanar space is similar to that of CuO-g-C_3N_4, therefore, the black particles must be CuO and the size of

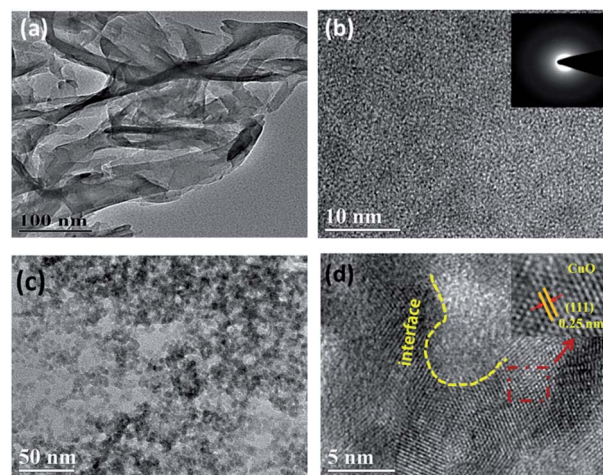**Fig. 2** TEM images of g-C_3N_4 (a) and CuO-g-C_3N_4 (c); HRTEM images of g-C_3N_4 (b) and CuO-g-C_3N_4 (d).

the CuO particles is approximately 6–8 nm, as presented in Fig. 2c. In addition, we can also observe from Fig. 2d that the (111) plane of CuO and amorphous g-C_3N_4 do not exist in isolation, and a mixed interface forms in the middle area, CuO and g-C_3N_4 are p-type and n-type semiconductors, respectively.[18] Therefore, an organic-inorganic hybrid p–n heterojunction has been successfully synthesized.

X-ray photoelectron spectroscopy (XPS) is generally used for the qualitative and semi-quantitative analysis of elements in the synthesized samples.[26,27] Fig. 3a shows that CuO-g-C_3N_4 has binding energy (BE) peaks at 932, 398, 287, and 532 eV, corresponding to Cu 2p, N 1s, C 1s, and O 1s, respectively. These
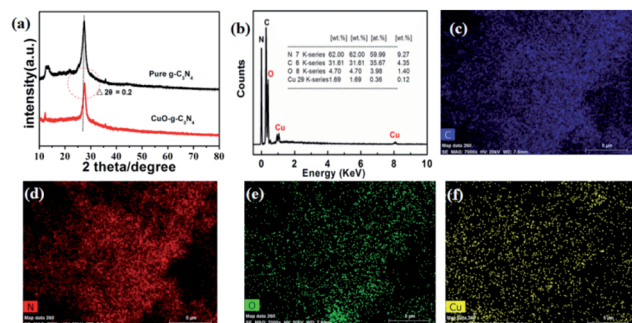

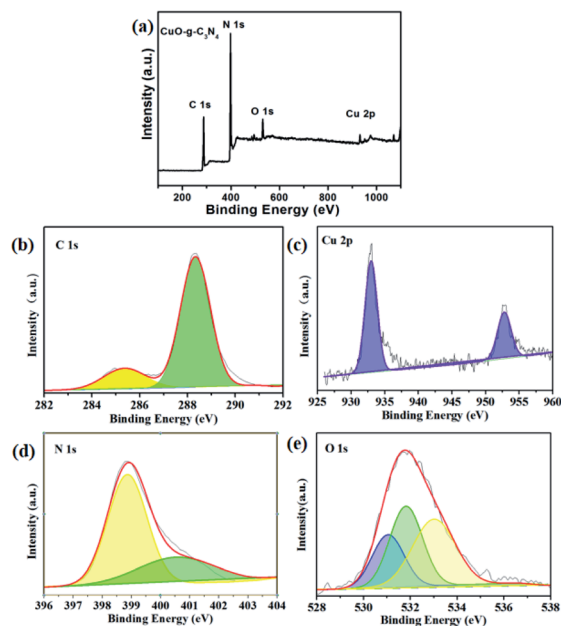**Fig. 1** XRD patterns (a), and EDS spectrum (b) for CuO-g-C_3N_4. The element-mapping of C (c), N (d), O (e), and Cu (f).

Fig. 3 XPS spectra of the synthesized CuO-g-C_3N_4 (a), sample survey and the high resolution XPS spectra for (b) C 1s, (c) Cu 2p, (d) N 1s, and (e) O 1s.

results also prove that CuO-g-C₃N₄ contains Cu and O, which is consistent with the EDS and corresponding element-mapping results. As shown in Fig. 3b, two BE peaks located at about 284.2 and 288.6 eV, are assigned to N–C=N and the SP² hybrid carbon atoms at the g-C₃N₄ surface.[5] Fig. 3c shows the high resolution XPS spectrum of Cu 2s. As shown in Fig. 3c, the BE peak at 953.9 eV belongs to Cu 2p$_{1/2}$, and the BE peak at 933.9 eV represents Cu 2p$_{3/2}$, proving that the Cu element exists in the form of +2 valence in the sample.[28–30] As observed from the N 1s spectrum in Fig. 3d, three different BE peaks appeared at 398.4, 400.6, and 404.3 eV, corresponding to the SP² hybrid nitrogen atom (C=N–C),[31,32] the C3 structure (N–C3), and the nitrogen atom in the hydrogen loading amino functional structure (C–N–H).[33] The XPS spectrum of O 1s in Fig. 3e illustrates that the O 1s peak can be deconvoluted into two peaks, the peak at 532.9 eV results from the adsorbed water molecules and OH⁻ adsorbed at the sample surface, while 531.4 eV comes from the O in CuO.[34,35]

The formed organic-inorganic hybrid p–n heterojunction at the CuO-g-C₃N₄ interface shows some changes in both the physical structure and optical properties of CuO-g-C₃N₄. These changes will have an important impact on the photocatalytic performance. RhB is used as a model molecule to assess the photoactivity of the as-prepared photocatalysts. The concentration of RhB does not show any changes without photocatalysts whether the light was on or off, indicating that RhB is very stable (Fig. 4a). When adding photocatalysts, for both cases, the concentration of RhB decreases gradually under dark conditions. This is a result of the adsorption caused by the ultrathin g-C₃N₄ nanosheet. When exposed to the light irradiation for 30 min, the degradation of g-C₃N₄ is 43.6%, and the degradation of CuO-g-C₃N₄ reaches 88.9%. The photocatalytic RhB removal of samples with different amounts of CuO loading were detected (Fig. S3, in the ESI†), the optimal CuO loading amount is 1.98%, (Fig. S3d†). The Langmuir–Hinshelwood kinetic formula was used to investigate the photocatalytic reaction dynamics.

$$-\ln \frac{C}{C_0} = kt \tag{1}$$

The −ln(C/C₀) versus t curve in Fig. 4b suggests that g-C₃N₄ and CuO-g-C₃N₄ follow first order dynamics. The rate constant (k) of RhB degradation for CuO-g-C₃N₄ is 0.0737 min⁻¹, which is about four times higher than that of the pristine g-C₃N₄
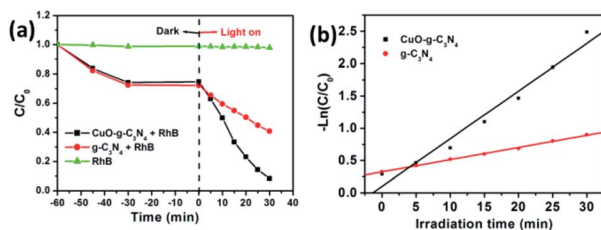
(0.0189 min⁻¹). The enhanced photoactivity of CuO-g-C₃N₄ may be attributed to the better visible light absorption capacity of CuO-g-C₃N₄.

As we know, light absorption is the premise of photocatalytic reactions. Therefore, UV-vis DRS spectra were used to assess the optical properties of these two samples. CuO-g-C₃N₄ has a stronger absorption in the UV-visible region (λ < 600 nm) than that of g-C₃N₄, and the absorption spectrum of CuO-g-C₃N₄ shows a red shift compared with g-C₃N₄ (Fig. 5a). This phenomenon suggests that CuO-g-C₃N₄ can capture visible light with a longer wavelength, which is mainly due to the close interaction between CuO and g-C₃N₄. As presented in Fig. 5b, the Eg values of CuO, g-C₃N₄ and CuO-g-C₃N₄ are about 1.45, 2.79 and 2.49 eV, respectively. Therefore, CuO-g-C₃N₄ can be excited to produce more photo-induced carriers. The valence band (VB) XPS were tested to evaluate the Ev of the different samples, from Fig. 5c, we can see that the VB positions of the CuO and g-C₃N₄ are 1.97 and 1.63 eV, respectively. Then, the conduction band (CB) position can be calculated using the formula $Eg = Ev − Ec$,[36] the CB positions of CuO and g-C₃N₄ were located at 0.52 and −1.16 eV, respectively (Fig. 5d).

After excitation, the photo-induced carriers may recombine and deactivate. The photoluminescence (PL) spectrum is a useful tool to investigate the recombination of photoinduced carriers at the interface. As shown in Fig. 6a, the PL intensity of CuO-g-C₃N₄ is obviously lower than that of the pristine g-C₃N₄, indicating that the formed heterojunction structure inhibits the recombination of the photoinduced carriers.[37] It is well known that the large specific surface area can provide more active sites for the photocatalytic reaction. Therefore, nitrogen adsorption–desorption isotherms were employed to evaluate the specific surface area of the prepared samples. The BET specific surface area of CuO-g-C₃N₄ was calculated to be 64.4 m² g⁻¹, which is much larger than that of the pristine g-C₃N₄ (34.7 m² g⁻¹) observed in Fig. 6b, we can conclude that the CuO-g-C₃N₄ can expose more active sites to enhance the photocatalytic activity.

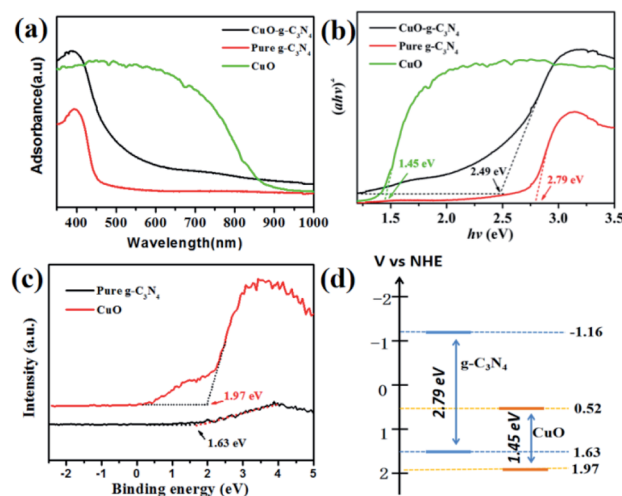Fig. 4 Comparison of the photodegradation of RhB for g-C₃N₄ and CuO-g-C₃N₄ (a), and the degradation kinetics (b) of g-C₃N₄ and CuO-g-C₃N₄.

Fig. 5 UV-vis absorption spectra (a) and the plots of (ahv)² versus energy (hv) (b) for g-C₃N₄ and CuO-g-C₃N₄; VB-XPS pattern (c); and the band structure of g-C₃N₄ and CuO (d).

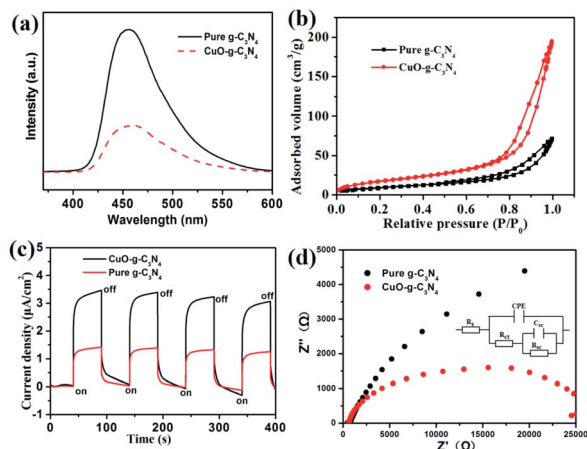**Fig. 6** PL spectra (a) and the nitrogen adsorption–desorption isotherms (b), current–time curves (c) and Nyquist plots (d) for g-C_3N_4 and CuO-g-C_3N_4.

Fig. 7 Comparison of the photoactivities of g-C_3N_4 (a) and CuO-g-C_3N_4 (b) in different photocatalytic systems ($\lambda > 420$ nm), comparison of the photocatalytic degradation of RhB (c) and NO removal rate (d) for CuO-g-C_3N_4, Mix-CuO/g-C_3N_4, and g-C_3N_4.

In addition to the inhabitation upon recombination, we believe that the formed heterojunction structure could also improve the transfer ability of the photoinduced carriers. This judgment is based on two reasons. On the one hand, g-C_3N_4 is an organic semiconductor, and its conductive performance is relatively poor. After coupling with metal semiconductor CuO, the conductivity of CuO-g-C_3N_4 is significantly improved. On the other hand, the built-in electric field close to the formed p–n heterojunction favors the faster transfer of electrons. PEC measurements were also conducted to prove the enhancement in photoactivity. As observed in Fig. 6c, the photocurrent density of g-C_3N_4 and CuO-g-C_3N_4 are 1.35 and 3.32 μA cm^{-2}, respectively. Furthermore, the photocurrent density of CuO-g-C_3N_4 is about 2.5 times as high as that of the bare g-C_3N_4. Electrochemical impedance experiments were performed to compare the conductivity of g-C_3N_4 and CuO-g-C_3N_4. The Nernst curves of CuO-g-C_3N_4 and g-C_3N_4 are shown in Fig. 6d, and the fitted equivalent circuits are also included in Fig. 6d. In the equivalent circuits, R_s is the electrolyte resistance, R_{ct} is the charge transfer resistance, CPE is the constant phase element, R_{SC} is the polarization resistance of the surface space-charge layer, and C_{SC} is the capacitance of the surface space-charge layer. The values of the R_{ct} and R_{SC} for the g-C_3N_4 and CuO-g-C_3N_4 electrodes were 480 and 718 Ω, and 237 and 482 Ω, respectively. This indicates that the combination of CuO and g-C_3N_4 forms the heterojunction structure and increases the conductivity.[38,39]

The reason for the enhanced photocatalytic performance of CuO-g-C_3N_4 is that the composite increases the visible light absorption capacity, inhibits the recombination of photo-generated carriers, and enhances the conductivity. Reactive species trapping experiments were used to investigate whether the photocatalytic process has been changed. KI, $K_2Cr_2O_7$, TBA, and PBQ were used as the photogenerated holes (h$^+$), photo-generated electrons (e$^-$), hydroxyl radicals ($\cdot$OH) and superoxide radicals ($\cdot O_2^-$), and scavengers, respectively.[40–42] As shown in Fig. 7, no change is observed for both samples after adding TBA, suggesting that $\cdot$OH is not involved in the
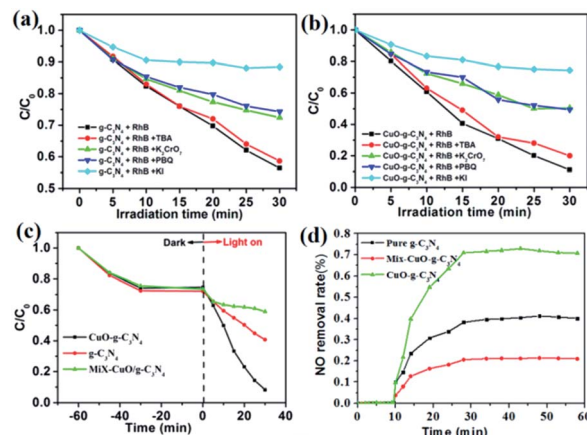
oxidation reaction. Therefore, neither CuO-g-C_3N_4 nor g-C_3N_4 can produce $\cdot$OH under visible light irradiation. Interestingly, the photocatalytic performances of these two samples all decrease when adding PBQ and $K_2Cr_2O_7$, indicating that $\cdot O_2^-$ and e$^-$ all participate in the reaction. When KI is added, the photocatalytic properties of these two samples decrease obviously, suggesting that h$^+$ is indispensable in the photocatalytic process. The whole capture experiments prove that the reaction is a photocatalytic oxidation process, and this reaction is mainly controlled by $\cdot O_2^-$ and the photoinduced carriers. Moreover, the experiments indicate that the combination of CuO and g-C_3N_4 does not change the photocatalytic pathway.

The enhanced photoactivity of CuO-g-C_3N_4 relative to the pristine g-C_3N_4 can be attributed to the formation of the organic-inorganic hybrid p–n heterojunction, along with the combination of CuO and g-C_3N_4. For comparison, Mix-CuO/g-C_3N_4 with the same CuO content (1.98%) was also prepared by mechanically mixing CuO nanoparticles (19.8 mg) and a g-C_3N_4 nanosheet (981 mg). As shown in Fig. 7c, under the same testing conditions, the photocatalytic degradation performance of Mix-CuO/g-C_3N_4 is even lower than that of the bare g-C_3N_4. The degradation of RhB is only 19.7% under visible light after 30 min of irradiation. The photocatalytic NO removal of different samples was tested (Fig. S3, in the ESI†), we can see that the result of photocatalytic NO removal (Fig. 7d) is very similar to that of RhB degradation, the optimal weight ratio of CuO and g-C_3N_4 is 1.98%, and the NO removal rate of CuO-g-C_3N_4 reaches 71.2% after 20 min of irradiation, which is about two times that of the pristine g-C_3N_4 (39.5%), Mix-CuO/g-C_3N_4 is the lowest, at less than 20% (Fig. 7d).

As observed in Fig. 8, the e$^-$ on the CB of CuO and g-C_3N_4 are excited under visible light irradiation. Two modes of electron transfer are considered, one is the double-transfer mechanism,[43–45] the other is the Z-scheme transfer mode. For the Mix-CuO/g-C_3N_4, the charge transfer follows a double-transfer mechanism because of the absence of a p–n heterojunction structure. The photoelectrons transfer from the CB top of g-C_3N_4 to the CB top of CuO, these e$^-$ are easily recombined with
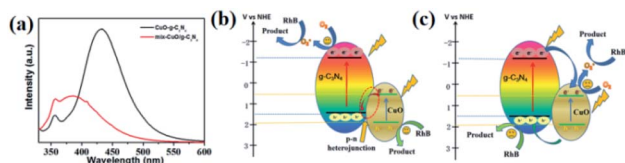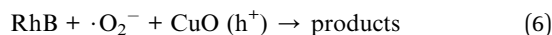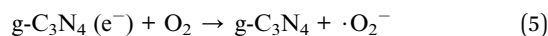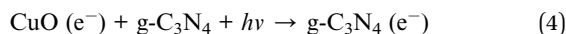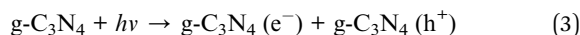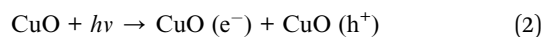
Fig. 8 Generation of ·OH using CuO-g-C$_3$N$_4$ and Mix-CuO/g-C$_3$N$_4$ (a), schematic diagram of the photoinduced carriers separation processes: (Mix-CuO/g-C$_3$N$_4$) double-charge transfer mechanism (b), and the (CuO-g-C$_3$N$_4$) Z-scheme mechanism (c).

h$^+$ at the VB of g-C$_3$N$_4$. Therefore, the visible photocatalytic degradation of RhB is only 19.8%. However, for CuO-g-C$_3$N$_4$, the built-in electric field close to the formed p–n heterojunction favors efficient electrons transfer of e$^-$ at the CB of CuO, which transfer through the built-in electric field and directly migrate to the VB of g-C$_3$N$_4$. This process obeys the Z-scheme transfer mode, the photoinduced carriers can be efficiently separated, thus the photocatalytic degradation rate of RhB can reach as high as 88.9%. From the active species trapping experiments, it is known that ·O$_2^-$ and photoinduced carriers play a significant role in the photocatalytic degradation of RhB and the electrons transfer follows a Z-scheme mechanism. We propose the following degradation process:

$$CuO + h\nu \rightarrow CuO\ (e^-) + CuO\ (h^+) \tag{2}$$

$$g\text{-}C_3N_4 + h\nu \rightarrow g\text{-}C_3N_4\ (e^-) + g\text{-}C_3N_4\ (h^+) \tag{3}$$

$$CuO\ (e^-) + g\text{-}C_3N_4 + h\nu \rightarrow g\text{-}C_3N_4\ (e^-) \tag{4}$$

$$g\text{-}C_3N_4\ (e^-) + O_2 \rightarrow g\text{-}C_3N_4 + \cdot O_2^- \tag{5}$$

$$RhB + \cdot O_2^- + CuO\ (h^+) \rightarrow products \tag{6}$$

4. Conclusions

In this work, a p–n heterogeneous structure, metal–organic hybrid CuO-g-C$_3$N$_4$ semiconductor was fabricated using a facile impregnation-calcination method. CuO-g-C$_3$N$_4$ exhibits a better photoactivity than that of the pure g-C$_3$N$_4$. The degradation rate of RhB, up to 88.9%, and NO removal rate reached 71.2% after being exposed to visible light irradiation for 30 min, the RhB degradation rate constant was about four times as high as that of the pure g-C$_3$N$_4$. Coupling CuO with g-C$_3$N$_4$ improves the visible light absorption, promotes the carrier separation, as well as enhancing the conductivity. Another reason for the improvement in the photocatalytic degradation is that the built-in electric field close to the formed p–n heterojunction switches the electron transfer mechanism from a double-charge transfer mechanism to a Z-scheme mechanism, resulting in an enhanced photocatalytic performance.

Conflicts of interest

There are no conflicts to declare.

Acknowledgements

Notes and references

1 K. C. Devarayapalli, K. Lee, H. B. Do, N. N. Dang, K. Yoo, J. Shim and S. V. Prabhakar Vattikuti, *Mater. Today Energy*, 2021, **21**, 100699.

2 S. V. Prabhakar Vattikuti, B. Purusottam Reddy, B. Chan and J. Shim, *J. Solid State Chem.*, 2018, **262**, 106–111.

3 X. Wang, K. Maeda, A. Thomas, K. Takanabe, G. Xin, J. M. Carlsson, K. Domen and M. Antonietti, *Nat. Mater.*, 2009, **8**, 76.

4 D. J. Martin, K. Qiu, S. A. Shevlin, A. D. Handoko, X. Chen, Z. Guo and J. Tang, *Angew. Chem., Int. Ed.*, 2014, **53**, 9240–9245.

5 Z. Chen, S. Pronkin, T.-P. Fellinger, K. Kailasam, G. Vilé, D. Albani, F. Krumeich, R. Leary, J. Barnard and J. M. Thomas, *ACS Nano.*, 2016, **10**, 3166–3175.

6 J. Zhang, M. Zhang, G. Zhang and X. Wang, *ACS Catal.*, 2012, **2**, 940–948.

7 M. Zhang, Y. Duan, H. Jia, F. Wang, L. Wang, Z. Su and C. Wang, *Catal. Sci. Technol.*, 2017, **7**, 452–458.

8 Z. Wang, C. Yang, T. Lin, H. Yin, P. Chen, D. Wan, F. Xu, F. Huang, J. Lin, X. Xie and M. Jiang, *Adv. Funct. Mater.*, 2013, **23**, 5444–5450.

9 T. Lin, C. Yang, Z. Wang, H. Yin, X. Lü, F. Huang, J. Lin, X. Xie and M. Jiang, *Energy Environ. Sci.*, 2014, **7**, 967–972.

10 C. Yang, Z. Wang, T. Lin, H. Yin, X. Lü, D. Wan, T. Xu, C. Zheng, J. Lin and F. Huang, *J. Am. Chem. Soc.*, 2013, **135**, 17831–17838.

11 F. Zuo, L. Wang, T. Wu, Z. Zhang, D. Borchardt and P. Feng, *J. Am. Chem. Soc.*, 2010, **132**, 11856–11857.

12 M. Wang, L. Sun, Z. Lin, J. Cai, K. Xie and C. Lin, *Energy Environ. Sci.*, 2013, **6**, 1211–1220.

13 G. Murali, S. V. Prabhakar Vattikuti, Y. K. Kshetri, H. Lee, J. K. R. Modigunta, Ch. S. Reddy, S. Park, S. Lee, B. Poornaprakash, H. Lee, Y. H. Park, J. Lee, S. Y. Park and I. In, *Chem. Eng. J.*, 2021, **421**, 129687.

14 K. C. Devarayapalli, K. Lee, N. D. Nam, S. V. Prabhakar Vattikuti and J. Shim, *Ceram. Int.*, 2020, **46**, 28467–28480.

15 F. Mou, L. Xu, H. Ma, J. Guan, D. R. Chen and S. Wang, *Nanoscale*, 2012, **4**, 4650–4657.

16 A. K. R. Police, S. V. Prabhakar Vattikuti, K. K. Mandari, M. Chennaiahgari, M. V. Phanikrishna Sharma, D. K. Valluri and C. Byon, *Ceram. Int.*, 2018, **44**, 11783–11791.

17 Z. Zhang and P. Wang, *J. Am. Chem. Soc.*, 2012, **22**, 2456–2464.

18 J. F. de Brito, F. Tavella, C. Genovese, C. Ampelli, M. V. B. Zanoni, G. Centi and S. Perathoner, *Appl. Catal., B*, 2018, **224**, 136–145.

19 K. Chiang, R. Amal and T. Tran, *Adv. Environ. Res.*, 2002, **6**, 471–485.

20 J. Luo, G. Dong, Y. Zhu, Z. Yang and C. Wang, *Appl. Catal., B*, 2017, **214**, 46–56.

21 J. Zhang, M. Zhang, C. Yang and X. Wang, *Adv. Mater.*, 2014, **26**, 4121–4126.

22 Q. Liang, Z. Li, X. Yu, Z. H. Huang, F. Kang and Q. H. Yang, *Adv. Mater.*, 2015, **27**, 4634–4639.

23 G. Zhao, G. Liu, H. Pang, H. Liu, H. Zhang, K. Chang, X. Meng, X. Wang and J. Ye, *Small*, 2016, **12**, 6160–6166.

24 J. Ghijsen, L. v. Tjeng, J. Van Elp, H. Eskes, J. Westerink, G. Sawatzky and M. Czyzyk, *Phys. Rev. B*, 1988, **38**, 11322.

25 H. Li, Z. Su, S. Hu and Y. Yan, *Appl. Catal., B*, 2017, **207**, 134–142.

26 W. Zhu, P. Liu, S. Xiao, W. Wang, D. Zhang and H. Li, *Appl. Catal., B*, 2015, **172**, 46–51.

27 K. Zhu, Y. Duan, F. Wang, P. Gao, H. Jia, C. Ma and C. Wang, *Chem. Eng. J.*, 2017, **311**, 236–246.

28 G. Li, N. M. Dimitrijevic, L. Chen, T. Rajh and K. A. Gray, *J. Phys. Chem. C*, 2008, **112**, 19040–19044.

29 S. Jung and K. Yong, *Chem. Commun.*, 2011, **47**, 2643–2645.

30 S. I. In, D. D. Vaughn and R. E. Schaak, *Angew. Chem.*, 2012, **124**, 3981–3984.

31 W. Wang, J. Fang, S. Shao, M. Lai and C. Lu, *Appl. Catal., B*, 2017, **217**, 57–64.

32 Y. Yu, W. Yan, W. Gao, P. Li, X. Wang, S. Wu, W. Song and K. Ding, *J. Mater. Chem. A*, 2017, **5**, 17199–17203.

33 X. Li, G. Hartley, A. J. Ward, P. A. Young, A. F. Masters and T. Maschmeyer, *J. Phys. Chem. C*, 2015, **119**, 14938–14946.

34 N. Zhang, X. Li, H. Ye, S. Chen, H. Ju, D. Liu, Y. Lin, W. Ye, C. Wang, Q. Xu, J. Zhu, L. Song, J. Jiang and Y. Xiong, *J. Am. Chem. Soc.*, 2016, **138**, 8928–8935.

35 N. Kruse and S. Chenakin, *Appl. Catal., A*, 2011, **391**, 367–376.

36 M. Zhou, G. H. Dong, F. Yu and Y. Huang, *Appl. Catal., B*, 2019, **256**, 117825.

37 X. Xin, T. Xu, J. Yin, L. Wang and C. Wang, *Appl. Catal., B*, 2015, **176**, 354–362.

38 C. Cheng, S. K. Karuturi, L. Liu, J. Liu, H. Li, L. T. Su, A. I. Y. Tok and H. J. Fan, *Small*, 2012, **8**, 37–42.

39 Z. Cai, F. Li, W. Xu, Y. Jiang, F. Luo, Y. Wang and X. Chen, *Nano Energy*, 2016, **26**, 257–266.

40 Z. Zhao, W. Zhang, X. Lv, Y. Sun, F. Dong and Y. Zhang, *Environ. Sci.: Nano*, 2016, **3**, 1306–1317.

41 L. L. Zhao, G. H. Dong, L. Zhang, Y. F. Lu and Y. Huang, *ACS Appl. Mater. Interfaces*, 2019, **10**, 10042–10051.

42 G. H. Dong, L. L. Zhao, X. X. Wu, M. S. Zhu and F. Wang, *Appl. Catal., B*, 2019, **245**, 459–468.

43 J. Di, J. Xia, S. Yin, H. Xu, L. Xu, Y. Xu, M. He and H. Li, *J. Mater. Chem. A*, 2014, **2**, 5340–5351.

44 C. Chang, L. Zhu, S. Wang, X. Chu and L. Yue, *ACS Appl. Mater. Interfaces*, 2014, **6**, 5083–5093.

45 S. F. Yang, C. G. Niu, D. W. Huang, H. Zhang, C. Liang and G. M. Zeng, *Environ. Sci.: Nano*, 2017, **4**, 585–595.